Journal of
Applied Physics

RESEARCH ARTICLE | NOVEMBER 08 2023

Reactive force field potential with shielded long-range Coulomb interaction: Application to graphene–water capacitors

Udoka Nwankwo ; Chi-Hang Lam ; Nicolas Onofrio

J. Appl. Phys. 134, 184502 (2023)
https://doi.org/10.1063/5.0173333

AIP Publishing

Journal of
Applied Physics

ARTICLE

pubs.aip.org/aip/jap

Reactive force field potential with shielded long-range Coulomb interaction: Application to graphene–water capacitors

Cite as: J. Appl. Phys. **134**, 184502 (2023); doi: 10.1063/5.0173333
Submitted: 21 August 2023 · Accepted: 20 October 2023 ·
Published Online: 8 November 2023

View Online Export Citation CrossMark

Udoka Nwankwo,[a)] Chi-Hang Lam, and Nicolas Onofrio

AFFILIATIONS

Department of Applied Physics, The Hong Kong Polytechnic University, Hong Kong SAR, China

[a)]**Author to whom correspondence should be addressed:** udoka.nwankwo@connect.polyu.hk

ABSTRACT

Electrode–electrolyte interfacial properties characterize the functioning of electrochemical devices, and reactive molecular dynamics simulations, using reactive force fields (ReaxFF) and charge equilibration (QEq) techniques, are classical atomistic methods for investigating the processes that govern the device properties. However, the numerical implementation of ReaxFF and QEq treats Coulomb interaction with a short-distance cutoff for computational speed, thereby limiting interactions among atoms to a domain containing only their neighbor lists. Excluding long-distance Coulomb interactions makes the description of electrostatics in large-scale systems intractable. We apply Ewald sum in the extension of ReaxFF to include long-range Coulomb (LRC) interactions and investigate the effect of the inclusion on the electrostatic and capacitive properties of graphene–water interfaces at different applied potentials in comparison with the original ReaxFF. The study shows that with the inclusion of long-range Coulomb, the capacitance amounts to $4.9 \pm 0.2\,\mu\mathrm{F\,cm^{-2}}$ compared with $4.4 \pm 0.2\,\mu\mathrm{F\,cm^{-2}}$ predicted by the original ReaxFF [with short-range Coulomb (SRC)]; thus, indicating that SRC underestimates the capacitance of water between graphene walls by 12% when compared with the $5.0\,\mu\mathrm{F\,cm^{-2}}$ predicted with the extended simple point charge (SPC/E) water model. Thus, the results indicate that LRC ReaxFF/QEq have the ability and advantage to model electrochemical processes at a more realistic Coulomb interaction description and foster the processing of the details about the operation of electrochemical devices than the SRC.

I. INTRODUCTION

Graphene–water systems have received tremendous attention in recent years owing to the tunable electrical properties[1] of graphene coupled with its sensitivity to the surrounding environment, dynamical wettability,[2] and the relevance of water to everyday natural life, including cases in ionic media and protein cavities,[3] fuel-cell membranes,[4] etc. The unique properties[5] of graphene and the polarizability of water under applied electrical stress rendered these electrochemical systems important for scientific, industrial, and technological applications. Example of applications include seawater desalination,[6] electric double-layer devices (EDL),[7] and supercapacitors.[8]

Interfacial water/electrode studies started in a drastically unrealistic form that models electrodes as smooth-hard walls with fixed uniform charge distributions and water as hard-sphere fluid.[9,10] Some other setbacks witnessed in modeling bulk electrolyte and interfacial boundaries between liquid electrolyte/electrode is the experimental and voltammetry[11] difficulty in taking measurements about interfacial changes at the atomic level. This problem was improved with the advent of atomic molecular dynamics (MD) simulation method. However, the challenge of accounting for a uniform external potential difference across the electrodes in an electrochemical system persisted. That forced researchers to maintain the old approach of enforcing constant charge densities of opposite polarities on the electrodes. A practice that failed due to nonphysical surges in temperature[12] and efforts toward resolving the problem led to the introduction of fluctuating charge methods,[13–18] which researchers applied in studying graphene/water,[19] copper/water,[20] and platinum/water[21] systems among others. Toward improving the approach, Siepmann and Sprik[22] proposed using a Gaussian charge function to determine the charge values that will fix the potential difference to a desired value. A more recent practice[20,21,23,24] in MD simulation involves perturbing the atomic electronegativity χ_0 by changing the electrode potential of the atoms in one of the electrodes from χ_0 to $\chi_0 + \Phi_0/2$ and the other from χ_0 to $\chi_0 - \Phi_0/2$. This would lead to a net electrochemical potential difference of Φ_0 volt across the electrodes and makes it easier to fix the external potential to desired values.

The functioning of electrochemical devices (especially capacitors, EDLs, and supercapacitors) is rooted in anions and cations adsorption in solvated media during the interfacial chemical interaction between electrodes/electrolyte and controlled by the nano-porosity/pore-size[25] of the electrode and the local interfacial structure of the liquid electrolyte.[12,26] In addition to the positive influence of fixing the potential based on the electrodes' nano-porosity/pore size, Li and co-workers[27] attributed structural changes at the application of an external potential to originate from the substantial difference in interfacial charge distribution leading to differential capacitance. Two independent authors, namely, Limmer[28] and Le Ma and co-workers,[29] respectively, linked differential capacitance in EDL capacitors to charge density ordering and charge-driven lateral structural evolution. These suggest that charge evaluation and the methods employed for the charge computation may affect/influence the characteristics of these devices under MD simulation. Among several molecular dynamics studies reported on metal/graphene and water interface reactions, the foci were on capacitance measurement,[19,30] interfacial structure organization and orientation of the electrolyte near the electrodes,[2,31–34] and capacitive behavior of the device.[27] However, the charge computation method and the effect it would have, if any, on the properties and behaviors of these devices received little/no attention. Here, we deployed the original QEq and ReaxFF that used short-distance cutoff to describe Coulomb interactions among atoms and compared the results with those of the combination of new ReaxFF described in this paper and the reformulated QEq that used the Ewald method to describe Coulomb interactions between atoms.

In this MD simulation, we extend reactive force field (ReaxFF)[35] potential to include long-range Coulomb interaction and used it to describe the interaction between atoms. ReaxFF is a classical interaction potential, which describes the total energy of a system of atoms as a sum of partial energy contributions from bonded (covalent) and non-bonded (van der Waals and Coulomb) interaction terms. The non-bond interactions are distance-corrected using a potential function called shielding interaction function[36,37] and seventh-order taper correction function.[38] The covalent counterpart, which is bond-order-dependent, determines the chemical environment of the atoms and controls the bond strength of the materials. The bond order is a function of the bond distance between two particles, and it changes as the local environment surrounding atoms is continually updated at each MD step but smoothly decays to zero as the separations between atoms increased beyond a user-specified cutoff. Details on ReaxFF are in Ref. 38. In most development and application of ReaxFF, the changing local atomic environment also requires an environment-dependent partial charge. The evaluation of the environment-dependent atom charges is attainable by coupling ReaxFF with the charge equilibration (QEq) technique developed by Rappé and Goddard.[13] These models (ReaxFF and QEq) enable the simulation of devices composed of dissimilar materials,[39] and they allow the description of interfaces and chemical reactions. However, numerical implementation of QEq and ReaxFF models includes Coulomb interaction only up to a short-distance cutoff for computational speed, a problem inherent to ReaxFF and limiting their description of Coulomb interactions only up to the cut-off region. We understand that Coulomb interaction is naturally long-range for non-covalent interactions (NCIs).[40,41] Such interactions exist in ionic and polarized systems where the motion of charged particles characterizes the electrical and electronic properties and behaviors of devices such as capacitors, electrochemical metallization (ECM) cells, EDLs, and batteries. Neglecting long-range Coulomb interaction affects the ability to describe charge distributions, polarization effects, the structure, and energy of a system. This is evident in solvated biological and biomolecular systems. For example, the cut-off sizes used in the Coulomb interactions strongly influence MD results on solvated polypeptides in which the stability of the α-helix configuration of peptide conformation is a function of cut-off size. Contrarily, the application of the Ewald technique in describing Coulomb interactions conserved the helical character of the peptide conformation.[42]

Based on the above background, we attempted to gain insights into the charge evolution on the electrodes, liquid water, and interfacial boundaries between the electrodes and liquid water as a function of applied potential using an environment-dependent charge and ReaxFF models that include long-range Coulomb (LRC) interaction. The implementation of our method in ReaxFF also serves as an example of the application of the Ewald technique. We discussed the effects of long-range inclusion has on the electrostatic and capacitive properties of the graphene/water capacitors by comparing results with the original method. We noticed some differences in the structural ordering and arrangements at the interfacial and bulk regions, as well as charge accumulations compared with the results obtained using the combination of original ReaxFF and QEq. The computed capacitances show that the short-range Coulomb (SRC) method underestimates the capacitance of the graphene–water capacitor.

Section II introduced and briefly discussed the models and computation methods applied in the simulations. Also, the system configuration is described in Sec. II. In Sec. III, we present and discuss the results and conclude in Sec. IV.

II. MODELS AND COMPUTATIONAL METHODS

A. Shielded long-range Coulomb interaction potential function

The interesting idea about the Ewald technique is that it allows the decomposition of a slowly decaying Coulomb potential function into a short-range component, which is rapidly convergent (rapidly goes to zero at large distances) in real-space and a long-range component, which decays quickly in reciprocal space.[43,44] Assuming unit point charges, the kernels of the Coulomb interaction potential are decomposed as given by Eq. (1). The second term on the right side of Eq. (1) is a smooth varying long-range function conveniently solvable in Fourier space. The function f must result in two fast decaying parts. In real space, f is often chosen to be an error function $\mathrm{erf}(x)$. However, in the reciprocal space, it is commonly retained as the Gaussian distribution function, because it is smooth, periodic, and representable by a rapidly convergent Fourier series,

$$J_{ij}(r_{ij}) = k_C \frac{1}{r_{ij}} = k_C \frac{1 - f(\zeta r_{ij})}{r_{ij}} + k_C \frac{f(\zeta r_{ij})}{r_{ij}}. \tag{1}$$

The parameter $\zeta > 0$ is the Ewald splitting parameter. It determines the spread or width of the representative functions. We focus on the real-space short-range component, i.e., the first term on the right side of Eq. (1), which is a complementary error function $\mathrm{erfc}(x) = 1 - \mathrm{erf}(x)$. Then, the total short-range real-space contribution ($\mathrm{V_{SRE}}$) to the Ewald-modified Coulomb potential energy of a N particle system and L periodic boxes is written as follows:

$$\begin{aligned} \mathrm{V_{SRE}}(r_{ij}) &= \frac{1}{2} k_C \sum_{i=1}^{\mathrm{N}} \sum_{j=1}^{\mathrm{N}} \sum_{m_\wedge = -\mathrm{L}}^{\mathrm{L}}{}' J_{ij}^{\mathrm{SRE}}(r_{ij}) \\ &= \frac{1}{2} k_C \sum_{i=1}^{\mathrm{N}} \sum_{j=1}^{\mathrm{N}} \sum_{m_\wedge = -\mathrm{L}}^{\mathrm{L}}{}' \frac{\mathrm{erfc}(\zeta |\vec{r}_{ij} + \vec{\mathrm{R}}|)}{|\vec{r}_{ij} + \vec{\mathrm{R}}|}, \end{aligned} \tag{2}$$

where $\vec{\mathrm{R}} = \sum_{\wedge = x,y,z} m_\wedge \vec{a}_\wedge$ is the position of each periodic unit box. $\vec{a}_\wedge$ is the box vector in each direction with $|\vec{a}_\wedge| = l$ implying a cubic box, $m_\wedge = (m_x,\ m_y,\ m_z) \in [-\mathrm{L},\ \mathrm{L}] \subseteq (-\infty, \infty)$ are integer values, and $\vec{r}_{ij}$ equals the displacement vector between particles i and j in the central box. The prime on the summation over periodic boxes is to indicate summation over all particle images (including self-images) in all periodic boxes with the exclusion of $i = j$ for $m_\wedge = 0$.

In numerical implementation, ζ is chosen so that $\mathrm{V_{SRE}}$ is restricted to particles in the box (i.e., $m_\wedge = 0$). This reduces the calculation of the real-space part of the potential to a normal minimum image convention (MIC) problem, which entails specifying a real-space short-distance cutoff $r_c \le l/2$. This approach is widely adopted and implemented across MD simulators such as large-scale atomic/molecular massively parallel simulator (LAMMPS),[45] Groningen machine for chemical simulations (GROMACS),[46] and nanoscale molecular dynamics (NAMD).[47] However, for sharp distribution of charges, the approach requires a large value of ζ and the inclusion of a sufficient number of reciprocal vectors (k-vectors) in the Fourier space summation part of the potential energy. The optimum ζ is chosen by balancing the error in (or the time needed to evaluate) the real and reciprocal space parts of the potential. Detailed expressions for the choice of ζ, k-vectors, and r_c are derived in Refs. 43 and 48–50. Therefore, letting $|\vec{r}_{ij}| = r_{ij}$ be the separation between two atoms in the central box, the short-range energy terms can be written as the followings:

$$\mathrm{V_{SRE}}(r_{ij} \le r_c) = \frac{1}{2} k_C \sum_{i=1,\, j \ne i}^{\mathrm{N}} \frac{\mathrm{erfc}(\zeta r_{ij})}{r_{ij}}. \tag{3}$$

The origin of the high repulsive behavior of the Coulomb interaction potential at close separations between atoms is probed under the Ewald summation technique. The system configuration consists of a NaCl dimer in a large simulation box of 100 Å, which is periodic in all directions. Figure 1 shows that the Fourier space component of the Ewald sum depicts the trend of the results obtained with empirical shielded Coulomb potential energy functions[36,37] and the exact solution based on Slater-type orbitals.[37] However, the overall repulsive behavior of the Coulomb interaction potential is observed to originate from the inverse distance in $\mathrm{V_{SRE}}$, which results in an unphysical energy contribution to the potential, especially at close atomic separations. Therefore, we modified the real-space contribution by introducing a shielding correction (function) proposed by Louwen and Vogt[37] to account for orbital overlap interactions at short distances between particles and expressed $\mathrm{V_{SRE}}$ as given in Eq. (4) for N particles. The force $\vec{F}_i$ on any ith particle is calculated following Eqs. (5) and (6). The erfc denotes complementary error function,

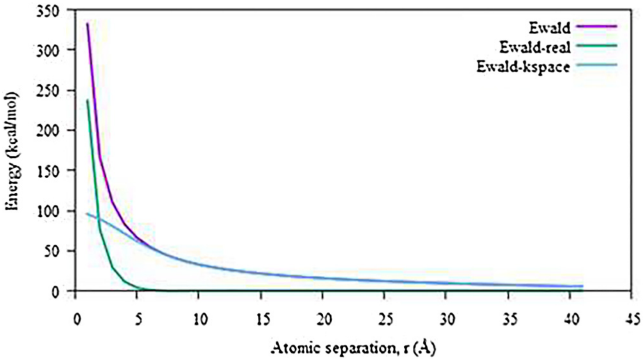

FIG. 1. Decomposition of the Ewald-modified Coulomb potential energy for NaCl. The energy value is inverted by −1 factor. The K-space contribution depicts the behavior of the Slater-type orbital evaluation of the Coulomb energy while the real-space component needs to be shielded.

$$\mathrm{V_{SRE}}(r_{ij} \le r_c) = \frac{1}{2} k_C \sum_{i,j}^{\mathrm{N}} \frac{\mathrm{erfc}(\zeta r_{ij}^{\mathrm{sc}})}{r_{ij}^{\mathrm{sc}}}; \qquad r_{ij}^{\mathrm{sc}} = \left(r_{ij}^3 + \gamma_{ij}^{-3}\right)^{1/3}, \tag{4}$$

$$\vec{F}_i = -\frac{\partial V_{\mathrm{SRE}}}{\partial r_i} = -\frac{\partial V_{\mathrm{SRE}}}{\partial r_{ij}^{\mathrm{sc}}} \frac{\partial r_{ij}^{\mathrm{sc}}}{\partial \boldsymbol{r}_i} = -\frac{\partial V_{\mathrm{SRE}}}{\partial r_{ij}^{\mathrm{sc}}} \vec{\Delta}_i r_{ij}^{\mathrm{sc}}, \tag{5}$$

$$\begin{aligned} \vec{F}_i = &\frac{r_{ij}}{(r_{ij}^3 + \gamma_{ij}^{-3})^{4/3}} \\ &\times \left(\mathrm{erfc}\left(\zeta \left(r_{ij}^3 + \gamma_{ij}^{-3} \right)^{1/3} \right) + \frac{2\zeta}{\sqrt{\pi}} \left(r_{ij}^3 + \gamma_{ij}^{-3} \right)^{1/3} e^{-\zeta^2 (r_{ij}^3 + \gamma_{ij}^{-3})^{2/3}} \right) \vec{r}_{ij}, \end{aligned} \tag{6}$$

where the superscript sc indicates r_{ij} is subject to shielding correction, k_C and ζ are the Coulomb constant and the Ewald splitting parameter determined in LAMMPS once the accuracy of the Ewald calculation is set, respectively. γ_{ij} is the shielding coefficient (parameter) in Å^{-1}.

The shielded correction is implemented in LAMMPS as a standalone pair interaction style called "coul/long/shielded." The effect of including the correction is tested on a NaCl crystal, having 0.40 and 0.35 Å^{-1} shielding (gamma) parameters for Na and Cl, respectively.[51] Figure 2 shows the plot of the energy against the

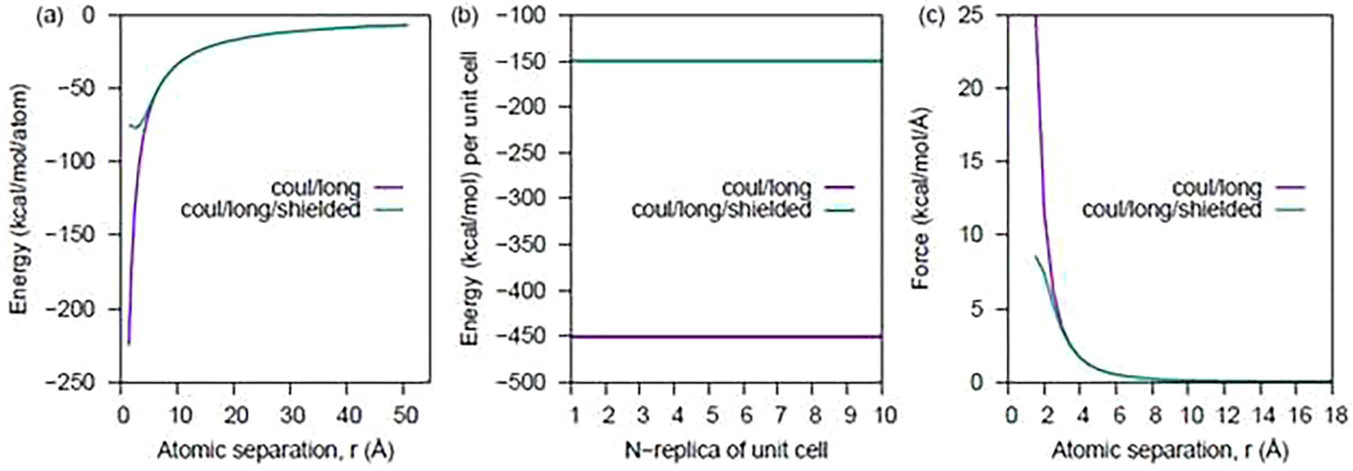

FIG. 2. Effect of shielding inclusion to long-range Coulomb on NaCl crystal (a) energy per atom, (c) force on an atom against atomic separation, and (b) energy per unit cell volume as a function of replicated unit cell with (without) shielded correction.

interatomic separation and the energy per unit cell volume against supercell size with/without the shielded function. The results depict the expected effect when compared with Refs. 36 and 37. In addition, the energy per unit volume as a function of the increased size of the supercell is constant as expected. The interaction energy as well as the forces [Fig. 2(c)] are consistently shielded at short interatomic distances, which is an improvement to the unphysically repulsive energy and forces recorded when atoms are at a small separation of the order of the vdW diameter or less.

B. ReaxFF model with long-range Coulomb interaction potential

ReaxFF with LRC inclusion is an improved model which modifies the non-bonded Coulomb interaction function [Eq. (7)] in the original ReaxFF non-bonded potential files in LAMMPS.[45] The modification is an application of the Ewald summation to the Coulomb energy and force functions. It replaced the shielded Coulomb interaction potentials with a shielded short-range real-space part [Eq. (4)] of the Ewald summation while calculating the long-range reciprocal space contribution in Fourier space without changes,

$$V_{\mathrm{Coul}}^{\mathrm{ReaxFF}}(r_{ij}) = \frac{1}{2} k_C \sum_{i,j}^{N} \left(\mathrm{Tap}(r_{ij}) \cdot \frac{q_i q_j}{(r_{ij}^3 + \gamma_{ij}^{-3})^{1/3}} \right). \qquad (7)$$

There are no long-range interactions in ReaxFF as implemented in LAMMPS. However, an opportunity to calculate atomic interactions at long-range Coulomb in reactive MD simulations is possible in LAMMPS through the hybridization of two or more pair potentials. Therefore, the "hybrid" styles commands alongside "reaxff" and "coul/long" pair interaction potentials in LAMMPS were used to compute Coulomb forces on atom *i* at various separations from atom *j*. The calculations show the inability of ReaxFF with/without (blue/purple curves of Fig. 3) long-range Coulomb to reproduce Ewald results (green curve in Fig. 3). The purple curve in Fig. 3 shows that the shielded Coulomb potential function [Eq. (8)] is incompatible and does not agree with the long-range part of Ewald sum. Therefore, the inability of the shielded direct

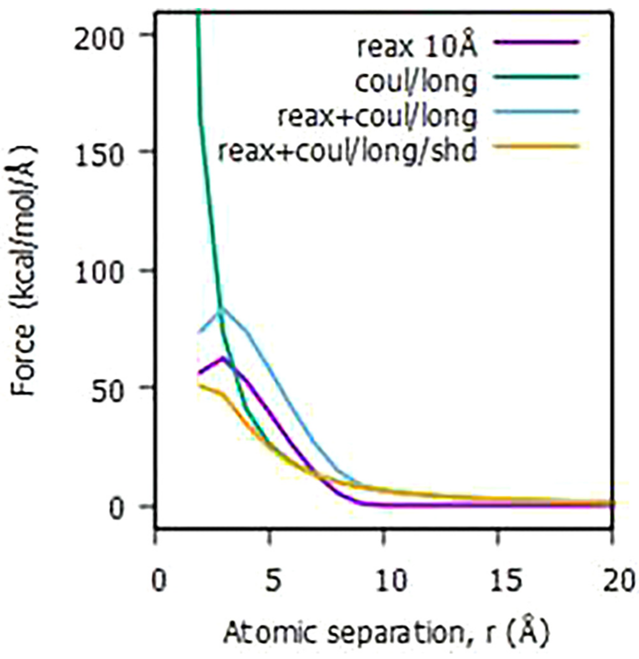

FIG. 3. Comparison of ReaxFF Coulomb forces on one of the Cl atoms in $MgCl_2$ molecule with and without long-range effect and shielded correction against coul/long (green curve) force.

Coulomb potential [Eq. (8)] to account for the real-space short-range part of the Ewald sum creates discrepancies in the Coulomb forces. We corrected this anomaly by implementing a shielded long-range Coulomb function within the ReaxFF non-bonded potential file in LAMMPS. The long-range Coulomb implementation [Eqs. (4)–(6)] is triggered whenever ReaxFF is hybridized with any "coul/long" pair interaction potential, which must require Ewald or particle–particle particle-mesh (pppm) reciprocal or k-space modified value in LAMMPS input run file. The orange curve in Fig. 3 shows an improvement accounting for the real-space short-distance part of long-range Coulomb.

We could see a striking agreement between the green and orange curves at distances below 10 Å cutoff. Without the shielded correction, the green and orange (reformulated ReaxFF) curves overlap, which are equivalent to analytically calculated force. We expect that with the long-range effect inclusion and shielding correction, a proper description of the slowly decaying Coulomb interactions between atoms in reactive MD simulation of large charged systems and electrochemical processes of atoms within a dielectric layer.

C. System configuration and simulation details

Structural configurations consisting of two parallel graphene layers (electrodes), each containing 28 fixed carbon atoms, were modeled in orthogonal supercells, which are periodic in x and y but fixed in z-directions with dimensions given as $7.77 \times 8.04 \times (17 + d_{\text{sep}})$ Å^3. The gaps between the electrodes $d_{sep} = 25.00$ Å were intercalated with water molecules to match the experimental density of a homogenous water fluid in the channel. We run two similar MD simulations on each system at 0.0 V with the large-scale atomic/molecular massively parallel simulator (LAMMPS)[45] at a time step of 0.5 fs. Constant NVT conditions were maintained using a Nose–Hoover thermostat with a damping factor of 100 fs and a temperature of 300 K for a total of 250 ps of accumulating statistics. The reactive force field (ReaxFF) model[35] was used to describe the interactions among atoms in the system configurations in which QEq evaluates the atomic charges. Our modified ReaxFF was hybridized with Ewald sum and applied to describe interactions among atoms in the systems in which QEqLR (charge equilibration method with long-range Coulomb)[52] was used to compute atomic charges. QEqLR is a reformulation of QEq[12] that replaced the Coulomb interaction term with a long-range electrostatic Coulomb interaction energy function defined through the Ewald summation. The details about QEqLR approach and its implementation are given extensively in Ref. 52. While the original model combination, ReaxFF and QEq, was denoted as the SRC interaction method, the later model combination, reformulated ReaxFF and QEqLR, was designated as the LRC interaction method. A 17.0 Å vacuum region was added along the z-directions of the supercells to suppress periodicity and to apply slab correction[53] equivalent to mimicking a 2D periodic boundary condition for the SRC calculations. The LCR interactions were described with the Ewald approach, adapted to the slab correction as described in LAMMPS. The simulations were repeated for various applied potential differences: $\Phi_0 = 1.0,\ 1.6,\ 2.0,\ 2.2,$ and 3.0 V following the earlier description.

III. RESULTS AND DISCUSSIONS

A. Electrostatic and capacitive properties

1. Electrodes response to applied voltage

To investigate the performance of the capacitor with and without long-range Coulomb interactions, first, we check how the electrodes with zero water intercalated between them and respond to applied potential in respect to charge accumulations. Emphatically before the simulation ran, the charge on each atom was zero. Table I shows the surface charge densities on the electrodes and they vary linearly with the applied potential difference. The results are consistent with those reported in Ref. 52 that shows SRC methods predict more charge at zero electrolyte/liquid water in between the electrodes. Subsequently, we intercalate the inter-electrode space with water and observe the surface charge density evolution at various applied potentials. The charge values or surface charge densities are due to the (i) differences in the electronegativity of the electrodes' atoms and the atoms of the water molecules and the interactions existing thereof and (ii) dipolar nature of water molecules. Note that the electrode charge values vary a little as expected since water has different orientations[34] at the liquid water/electrode interfaces. Additional source of variations is attributed to the electrode charges' adjustment in response to the local field changes and charge fluctuation due to the water atoms described by a reactive field function other than the SPC/E-modeled water with fixed oxygen and hydrogen charges.

2. Time evolution of surface charge at the electrode

The water atom charges fluctuate a little over time. The average partial charges on the water atoms are predicted at $q_H = 0.367 \pm 0.020\ e$ ($q_O = 0.743 \pm 0.021\ e$) for the SRC models and those of the LRC models are $q_H = 0.353 \pm 0.021$ e($q_O = 0.715 \pm 0.021\ e$). These values are between the experimentally obtained charges[12] $q_H = 0.325\ e$ and the SPC/E water charges $q_H = \ 0.4238\ e$ (available in the supplementary material of Ref. 19), where $q_O = 2q_H$. Note that the SRC and LRC predicted charges for water atoms may differ sparingly in different calculations and from the results obtained experimentally or through the SPC/E water model; the difference would result from the variations in parameters of the force field used in the calculations. Observe that q_O does not strictly equal $2q_H$; that is, the consequence of the fluctuating

TABLE I. Total surface charge density (μC cm^{-2}) on the electrodes at various applied potential and with no water intercalated between the electrodes. LE (RE) = left electrode (right electrode).

	LRC		SRC	
Φ_0	LE	RE	LE	RE
0.0	0.000	0.000	0.000	0.000
1.0	1.103	−1.103	2.082	−2.082
1.6	1.764	−1.764	3.331	−3.331
2.0	2.206	−2.206	4.164	−4.164
2.2	2.426	−2.426	4.580	−4.580
3.0	3.308	−3.308	6.246	−6.246

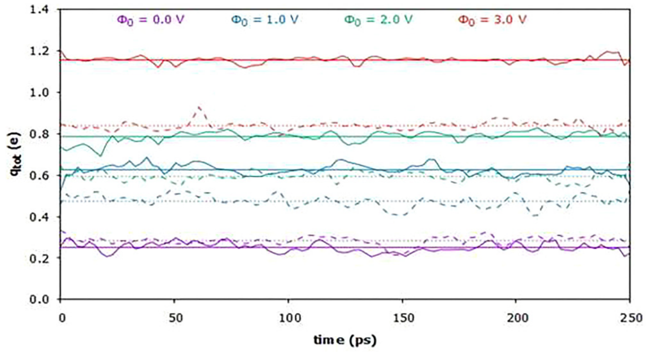

FIG. 4. Time evolution of total q_{tot} and average total $\langle q_{tot} \rangle$ electrode surface charge as a function of applied voltage Φ_0; fluctuating dashed and solid lines represent SRC and LRC, respectively, while dotted and solid horizontal lines are the corresponding average total surface charges.

charge technique where the atom charges depend on their local environment; however, while the electrodes offset the deficit in the water atom charges, the overall charge of the system is to the order of 10^{-6} zero. Figure 4 describes the total surface charge on the negative (positive) electrode, which is the sum of individual atomic charges as a function of simulation time evaluated at various applied voltages. Except for the zero potential, LRC predicts more surface charges on the negative electrode than the SRC, thereby elucidating the influence of allowing long-range Coulomb in the presence of applied potential. Combining this result with Fig. S2 in the supplementary material suggests that LRC orders more structure near the surface of one of the electrodes than the SRC. The atom charges, including those of the solvent, fluctuate with time; therefore, the total $\langle q_{tot} \rangle$ fluctuates. However, the averages q_{tot} of these fluctuations indicated on the plots by dotted and solid horizontal lines for SRC and LRC, respectively, after a long equilibration, are the actual quantity needed for quantifying the capacitance of the capacitor.

3. Electrode surface charge distribution

Figure 5 is a distribution (histogram) of the partial charge on carbon atoms of the positive (solid lines) and negative (dashed lines) electrodes, averaging over the entire statistic production time. The distribution is non-Gaussian but a bimodal,[54] and it exhibits similar behaviors as the non-Gaussian charge distribution recorded in a simulation by Demir and Searles;[55] however, the systems contain ionic-liquid electrolytes different from only liquid water reported in this article. The non-Gaussian charge distribution, perhaps, delineates some differences between dynamic and fixed charge models,[56] such as charge adjustments in the former to respond to local charge density fluctuations between water atoms or an electrolyte and the electrode atoms. Evidence in the plots is a drift of the mean of the histograms away from zero at increasing the potential difference between the electrodes. That shift is more pronounced during electrode polarization with LRC than the SRC, which indicates that the LRC could be encouraging charge overscreening[57] that delivers more counter charge than the absolute value of the electrode charges at the interfacial layer more than the SRC, especially when ionic liquids become the electrolyte. We analyzed the bimodality observed on the electrode's surface charge distributions on the electrode' atoms, which are due to the interfacial water molecules or atoms' interaction with the electrode atoms. The figure shows varying amplitudes, which explains the

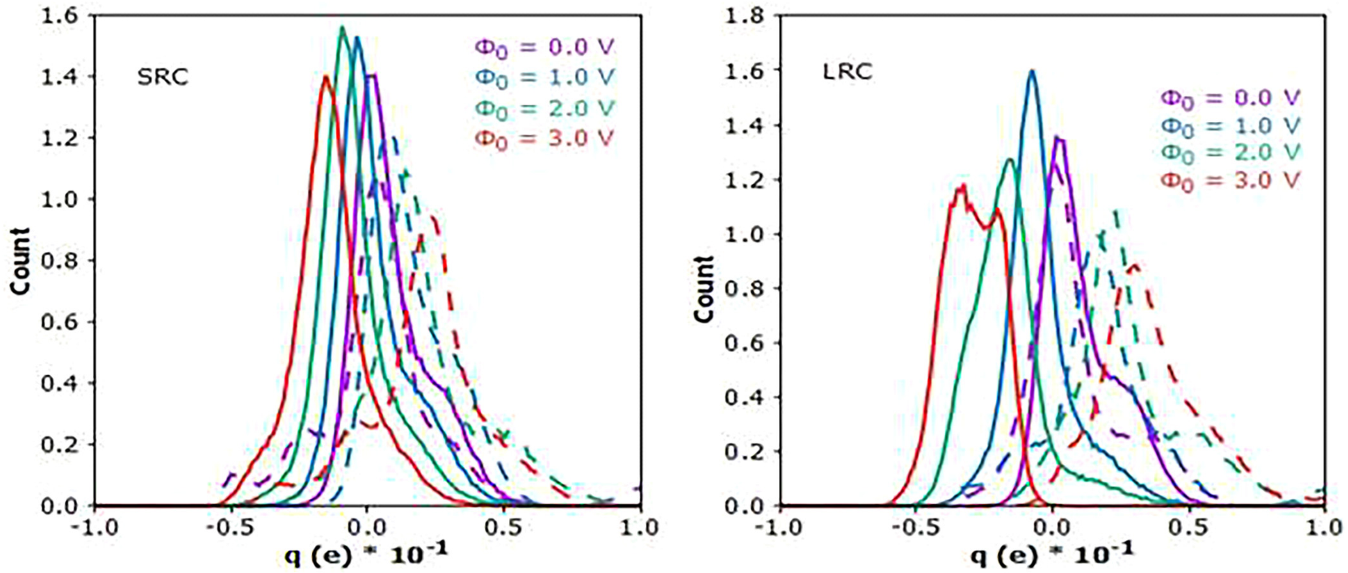

FIG. 5. Distribution of graphene atom charges for positive (solid lines) and negative (dashed lines) electrodes at various applied potential difference.

fluctuation in the number of electrode atoms possessing certain partial charges due to interfacial water molecules/atoms interaction. The bimodal distribution is a consequence of the ordering/orientation[54,58] of the water molecules seen on the OH bonds' responses to the applied field, which could be tilting toward the graphene surface or away from it.

4. Integral capacitance of the device

Figure 6 shows the interfacial average surface charge density $\langle\sigma\rangle$ on the positive electrode as a function of the applied potential. As expected, the predicted average surface charges or surface charge densities are in linear correspondence with the applied potential, which results in a constant value for the integral capacitance. The capacitance is defined here according to Refs. 59–61. And for easy calculation, it is simplified as a ratio of average surface charge density $\langle\sigma\rangle$ to potential difference across the electrodes (in this case, the applied voltage values and not the potential drop of the electrode relative to the bulk region of the system),

$$C_{int} = \frac{\langle q_{tot}\rangle}{A\Phi_0} = \frac{\langle\sigma\rangle}{\Phi_0}. \tag{8}$$

$\Phi_0 = \Phi_0^{+} - \Phi_0^{-}$ is the potential difference applied across the electrodes, which equals the overall (sum of the) potential drops between the bulk of the liquid water and the individual electrode surface. From the plot (Fig. 6) and linear regression of the data, the capacitance recorded is 4.4 ± 0.2 and $4.9 \pm 0.2\,\mu\text{F cm}^{-2}$ with QEq and QEqLR, respectively. These results point to the accuracy of the method employed for the description of Coulomb interaction between atoms of the electrodes and the water molecules and show that more charges are accumulated at the graphene electrode with LRC than with SRC. The error bars represent the standard error associated with each method. The overlap of the standard error bars shows the extent of uncertainty or variation in the data, and it suggests that the difference between the two methods is within the range of expected variability. The results are comparable with $5.0\,\mu\text{F cm}^{-2}$ recorded for liquid water with an extended simple point charge (SPC/E) model, intercalated between graphene electrodes, and studied using MD simulations.[19] The substantial difference between the short-distance and long-range Coulomb models is not surprising since the latter includes a more realistic description of the interaction field between atoms in a system. The intercept on the vertical axis corresponds to the interfacial surface charge density due to the interaction between the atoms of the electrode and the water molecules at a zero applied field for the system. The integral capacitance is a measurable quantity for quantifying the energy density of supercapacitors, which carries the performance index of the capacitor. By the results obtained and comparisons made, SRC under-predicts this quantity by 12%. This is a suggestion that with the addition of the long-range effect through Ewald summation, ReaxFF within LAMMPS can accurately model the capacitance of the graphene–water system than the original ReaxFF with truncated Coulomb interaction in comparison with the SPC/E water model. It is also an indication that the new model has a better learning and representation of the electrostatic properties and behavior of the simulated system. Practically and in application, 12% improvement suggests that the new method within the framework of ReaxFF application is more reliable and closer to previously predicted value by other generally accepted method (such as SPC/E) and could be more useful for design optimization, analysis, and other application where accurate capacitance modeling and use of ReaxFF is important or employed. Though the reformulated method is not developed and tested specifically for water confined with graphene-walled electrodes, meaning it can be applied to any system, extrapolating the 12% improvement to devices of different materials could introduce uncertainty knowing very well that the underlying mechanisms governing capacitance might differ for diverse systems. The gain could be influenced by some factors such as the charge estimation method used for charge computation since no two-charge scheme give the same result; the presence of a solute in the liquid water, which can influence the charge density at the interfacial region; and the parameters in the ReaxFF potential and Ewald summation function such as the Ewald splitting parameter, which differs for every system and is computed in LAMMPS based on the tolerance or accuracy one sets. Another limitation is the computation cost, particularly when the new method is combined with QEqLR (Ref. 52 and its supplementary material for the simulation time with QEqLR against QEq).

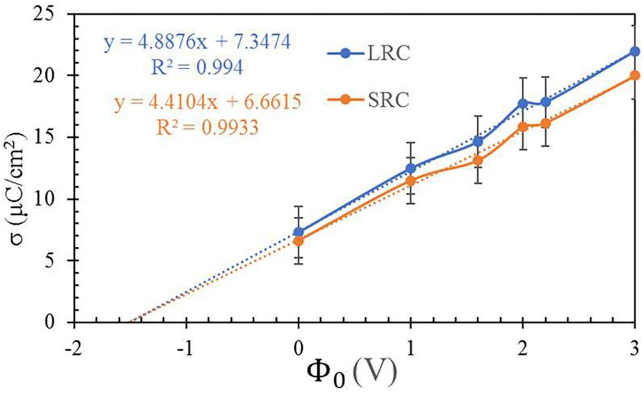

FIG. 6. Surface charge density on the positive electrode as a function of the applied potential difference with standard deviation expressed as error bars.

What would one expect if the gap size and lateral dimensions were varied? Varying the electrodes' lateral dimension and gap size between them may not bring new knowledge into understanding the capacitor's capacity because that would mean varying the surface area and the distance between the electrodes, which are among the factors known to be affecting the capacity of a capacitor. However, examining the capacity for the gap size variation for SRC and LRC has been done on Cu–Cu parallel plate capacitor, though with no dielectric material intercalated between the electrodes and analyzed with a focus on an electrode's total surface charge.[52] The capacitance is in direct relation with the surface charge density; therefore, examining the surface charge is as good as investigating the capacitance since the applied potential difference as well the electrodes' surface areas are the same for SRC and LRC. In the study, the exponentially decaying trend of the total surface charge as a function of gap between the electrodes was qualitatively compared with those given in Refs. 62–64. The net surface charge on the electrodes for the QEqLR (LRC) exhibits the long-range Coulomb effects as the gap increases; that is, the electrode's total surface charge as a function of the gap followed the order as those observed on an electrode in a triboelectric nanogenerator,[62] near the cathode surface in surface flashover model,[63] and on the electrodes in an integral equation theory of an electric double-layer device.[64] On the contrary, with the QEq (SRC) model, the total surface charge drops sharply around the cutoff and beyond the cutoff, the charge distribution remains a constant, suggesting that the electrodes even when they are well separated will feel a force from each other due to the charges they possess. A plot ratio of these surface charges to applied potential difference against separation would give a similar exponentially decaying curve as that recorded experimentally for a capacitor in Ref. 65. These results delineate the deviation from SRC and shows that long-range Coulomb via the Ewald summation is a better way to describe the Coulomb electrostatic interaction and could mean that some imbalances (such as an atom not seeing compensating charge) and surface artifacts imposed by a cutoff in charge distribution on the layers of the electrodes are eliminated.

5. Charge density distribution

Atomistic simulation uses the fine structures and local arrangements of atoms and molecules to calculate the electrode/electrolyte interface properties. The local charge density ρ_q of the electrolyte as a function of the coordinate z in the direction normal to the electrode surface follows Eq. (9) as is given by

$$\rho_{qj} = \int \rho_i(z')dz' = \frac{1}{\mathrm{V}}\left[\sum_{i=1}^{N} q_i\right]_{z_0+jh_z}^{z_0+(j+1)h_z}. \tag{9}$$

Here, the density of the fluid is inhomogeneous especially at the interfacial regions and, therefore, generates inhomogeneous partial charge distribution for the atom species in the systems. Consequently, the charge density distribution $\rho_i(z) = \sum q_i \delta(z - z_i)/\mathrm{V}$ (δ denotes the Dirac delta function) of a water molecule between the electrodes arises from a set of point charges q_i and is calculated by binning the position of the atoms with their associated partial charges into small rectangular bins along the z-direction. V equals the area A_{xy} of the xy-plane multiplied by the bin size h_z, and it equals the bin volume. The lower and upper limit of each bin is $z_0 + jh_z$ and $z_0 + (j+1)h_z$ with $0 \le j \le nbins$ (number of bins). q_i are the charge of ith atoms bounded by the bin walls, within which the charge density ρ_q relating to bin j is computed. A case where the atom species possess equal partial charges, the charge density is simply $\rho_q = \sum \rho_\alpha \cdot q_\alpha$ (ρ_α and q_α are the number density and the partial charge of species α).

Figure 7 shows the charge density distribution along the electrodes' normal surface (z-direction) at different potential differences. It portrays charge oscillations near the surfaces of the electrodes with alternating negative and positive peaks, which extend to about 5 Å into the system the electrolyte in zero and non-zero applied voltages. For all Φ_0, the plots compare the short- and long-range Coulomb (SRC and LRC) results. The two models gave an identical pattern of charge distributions except for a minor difference where LRC seems to project more negative charge to the left electrode surface than the SRC at the non-zero potentials. As an external potential difference is applied, the system becomes polarized. At 0.0 V, the charge distributions exhibit symmetry between the negative and positive peaks co-existing at both electrode surfaces, which were the consequence of the interactions between the graphene electrodes and the atoms of the water molecules. On switching the voltage to various values, the systems became polarized, and an excess positive charge developed near the right electrode leading to negative atom charges near the left electrode in compliance with the applied field. These charge distributions at interfacial regions generate additional electric fields, which add to those of the applied voltage and influence the orientation of the water molecules toward and away from the positive electrode breaking the symmetry (Fig. S2 in the supplementary material) of the density profile.

6. Poisson potential and differential capacitances

Proceeding further to characterizing the device leads to a more complex electrostatic potential file, which could be solved by evaluating the Poisson equation along the surface normal to the electrodes. Solving the Poison equation allowed the computation of the evolution of the potential across the device. The electrostatic potential and the ionic distribution relate through the Poisson–Boltzmann equation, which in the anisotropic z axis that is normal to the electrode surface is presented in Eq. (10). The c_+ and c_- are positive and negative ion concentrations,[57] respectively, and $Z = |Z^+| = |Z^-|$ is the valency of the ions,

$$\frac{\mathrm{d}^2\Phi}{\mathrm{d}z^2} = -\frac{Ze}{\varepsilon_0}[c_+ - c_-] = -\frac{\rho_q(z)}{\varepsilon_0}. \tag{10}$$

This second-order non-homogeneous differential equation is solved while recognizing two boundary conditions depending on the method[66] employed for calculating the potential. Here, the solution and potential across the electrodes are sorted analytically with the one-sided Green's function method, which seems to be a method favorable for researchers[66–68] to obtain the complementary homogeneous and the particular integral solutions that yield the following general solution:

$$\begin{aligned}\Phi(z) &= -\frac{1}{\varepsilon_0}\int_0^z \int_{z'}^z dz'' \rho_q(z')dz' + C_1 z + C_2 \\ &= -\frac{1}{\varepsilon_0}\int_0^z (z - z')\rho_q(z')dz' + C_1 z + C_2.\end{aligned} \tag{11}$$

The final Poisson potential is evaluated numerically through the numerical integration method (specifically the trapezoidal rule), which allows the binning of the atomic positions and the charge density distribution as employed in Ref. 66. ρ_q is the average charge density across the cell, including contribution from the electrodes. C_1 and C_2 are integration constants for the electrodes located at z_0 and $z_{d_{sep}}$, usually at $z_0 = 0$ and $z_{d_{sep}} = d_{sep}$, relating to $\mp\Phi_0/2$ volt perturbation applied alternately to both electrodes, respectively.

Figure 8 gives the electrostatic potential calculated with the Poisson equation illustrated above. Note that the potential fluctuates in the two models and oscillates heavily near the surfaces of

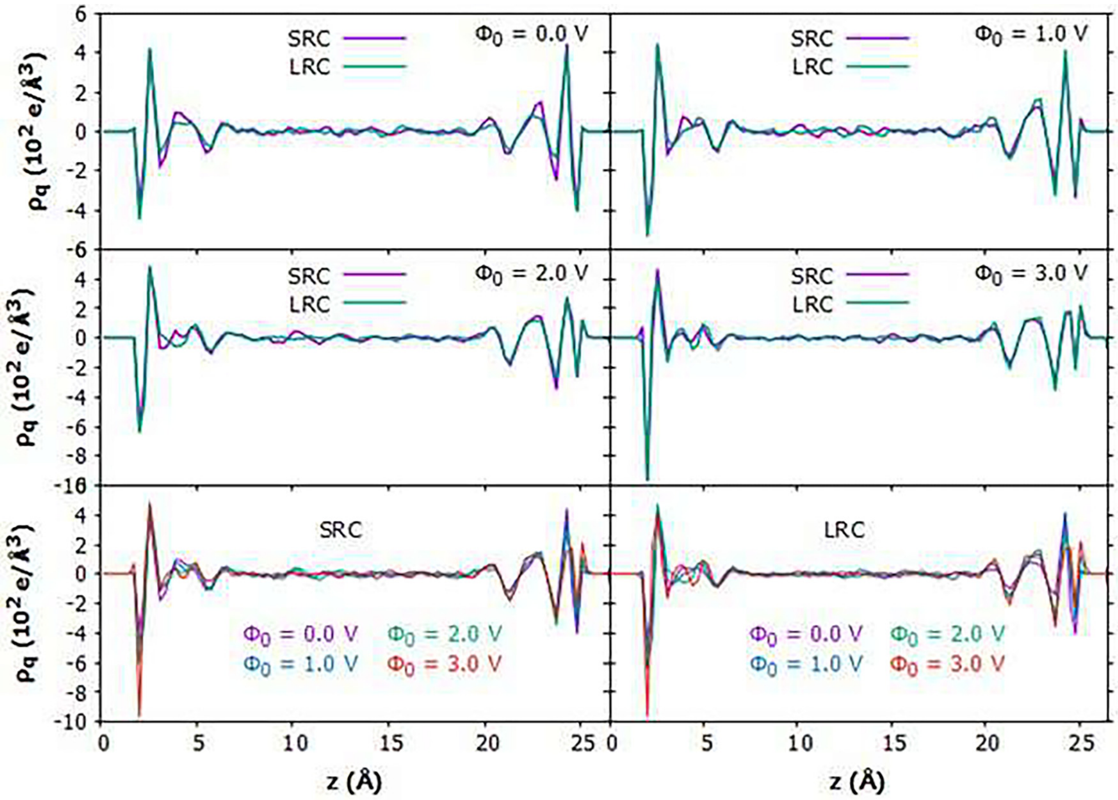

FIG. 7. Charge density profile of system at various Φ_0 applied across the graphene electrodes for the SRC and LRC description of interaction among atoms.

the electrodes on which it drops. The oscillations extend to about 7.5 Å measuring from the electrodes before exhibiting constant potential in the interior around the bulk region of the system. Although little ripples exist in the bulk portion of the system, not only with the potential but also on the water and charge density profiles. These are due to the prevailing slow relaxation of the water, which would require long simulation times and the accumulation of more statistics to generate smooth distribution profiles. The profound near-electrode surface oscillations are due to the ordering of the water molecules in these regions, as depicted in the water density and charge profiles. The SRC and LRC approach behave alike in oscillation patterns; however, some significant differences abound in the responses to applied voltages. The differences are related to the average partial charges on the surfaces of the electrodes since LRC tends to stabilize charge separation in the interfacial layers to a much greater extent than the SRC. Notice that the potential shows constant steepness typical of a bulk dielectric system under an applied electric field; with LRC predicting higher numerical values at the positive left electrode and lower values at the negative right, the SRC yields the reverse results. It seems like LRC tends to stabilize charge separation (screening) at the interfacial layers to a much greater extent than the SRC when judged by the potential drops and the differential capacitance at the electrodes.

The differential capacitance C^s_{diff} is a single-electrode capacitance calculated as the ratio of the average surface charge density $\langle\sigma\rangle$ on one of the electrodes to the potential drop $\Delta\Phi^{\pm}$ across the same electrode relative to the center (bulk region) of the capacitor. It gives details of the solvation, ion or charge absorption, and general physiochemical processes happening at the interfacial region more than the integral capacitance that informs about the energy storage density. This quantity is always written in a compact form as follows; Φ_{bulk} is the Poisson potential at the center of the capacitor,

$$C^s_{diff} = \frac{\partial\langle\sigma\rangle}{\partial\Delta\Phi^{\pm}},$$

where

$$\Delta\Phi^{\pm} = \begin{cases} \Phi^{+} - \Phi_{bulk} \\ \Phi^{-} - \Phi_{bulk} \end{cases}. \tag{12}$$

The slopes of the linear fits in Fig. 9 give the differential capacitance as $C^{-}_{diff}(C^{+}_{diff}) = 10.7(9.9)\,\mu\text{F cm}^{-2}$ and $C^{-}_{diff}(C^{+}_{diff}) = 7.0(16.2)\,\mu\text{F cm}^{-2}$ for the LRC and SRC models, respectively. The results show that the capacitance is higher on the positive electrode than on the counterpart for the SRC. For LRC, the

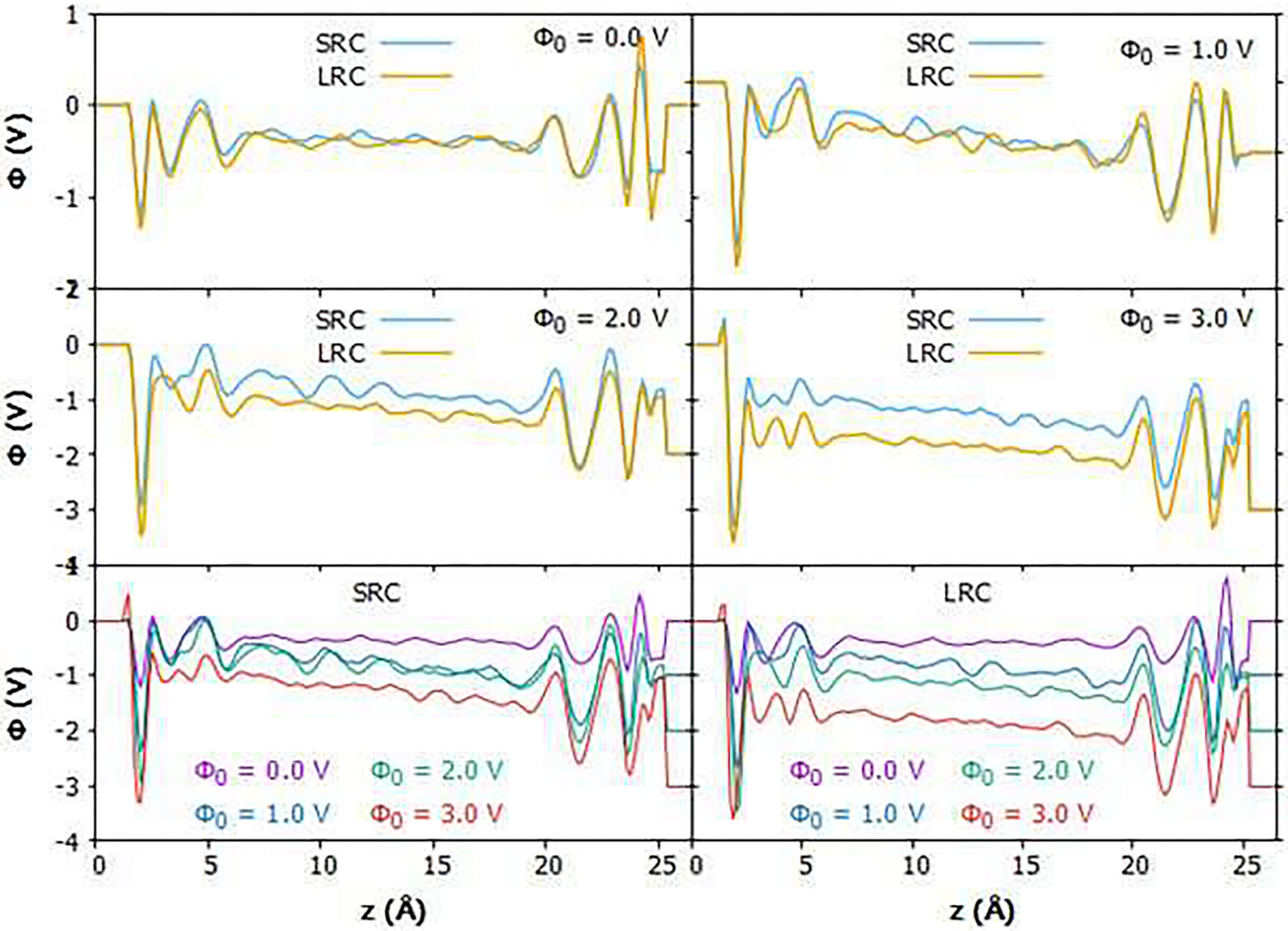

FIG. 8. Poisson potential profiles across the simulation cell calculated at various applied voltages Φ_0 and compared between the SRC and the LRC.

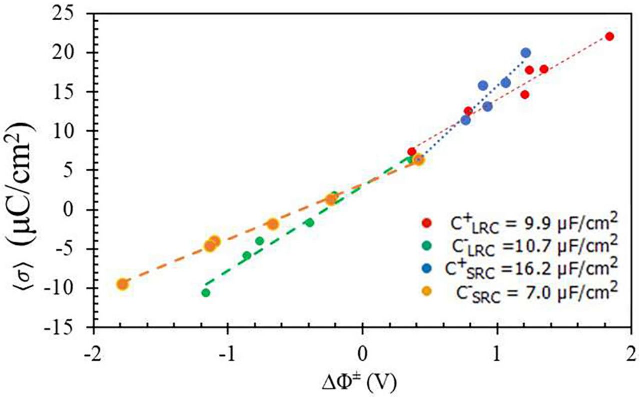

FIG. 9. Surface charge density as a function of interfacial electrostatic potential drop relative to the bulk region. The slopes of the linear fits give the differential capacitance.

capacitances are close but slightly higher on the negative electrode than on the opposing one. It also shows that the average surface charge density to electric potential drop ratio on the surfaces of the electrodes is distributed equitably with the LRC than is with SRC.

Checked against the literature,[69] the calculated C^s_{diff} of graphene super capacitors with an ionic-liquid electrolyte have slightly higher negative electrode capacitance than the positive electrode in all systems studied. Reference 27 also computed the negative electrode to have higher differential capacitance than the positive one for a graphene/ionic-liquid electrolyte system; the same trend was observed in other works[69–71] done with graphene electrodes and ionic liquids. Against these checks, LRC seems to predict better information about the electrodes than SRC.

IV. CONCLUSIONS

This report is an application of Ewald sum in the ReaxFF algorithm, to account for long-range effects in the description of the electrostatic Coulomb interactions among atoms. Its main objective is to explore the long-range Coulomb effects on electrochemical device properties and also to mitigate the effects of truncated Coulomb interactions in ReaxFF pair interaction potential as implemented in the LAMMPS simulation code. The original ReaxFF and QEq descriptions of Coulomb interaction are accurate for systems whose atomic spreads are within the user-specified cut-off distance (usually 1.0 nm) allowable for atoms to interact. Otherwise, the interaction of an atom with others in large systems is only regional, and it only extends to the particles in the neighbor list of the focused particle at any MD time step. It does not matter whether the Coulomb force or energy has sufficiently decayed to zero; energy contributions beyond the said cut-off radius are ignored. To perform MD simulations, for which the separation between the electrodes is more than 1.0 nm, we included a long-range effect (via Ewald summation) in the Coulomb interaction among atoms in the ReaxFF model and used it alongside QEqLR method. The models are applied to investigate the long-range Coulomb effect in the reactive MD simulation of water between sheets of graphene electrodes, for which results were compared against those of the original QEq and ReaxFF. Simulations were carried out for the old and new models at various applied potential differences. The simulations with the new method were at a bit more computation time than the original method. The simulation time difference originates from the QEqLR method, which required more time to compute atom charges; otherwise, the time difference between the original ReaxFF and the reformulated ReaxFF within LAMMPS is insignificant. Runtimes to obtain charges with the QEq and QEqLR are shown in Fig. S5 in the supplementary material of Ref. 52.

At all inter-electrode spacing, water shows strongly stratified lamellae of density modulations in the direction normal to the electrode surfaces. We observed related results from both models; however, a closer inspection unveils some differences. LRC predicts a little more structured solvation around the interfacial graphene walls than was seen with SRC, suggesting that the water molecules tilt more to the electrode with LRC. On applying a non-zero potential across the device, LRC reveals a clear relative shift between the oxygen and hydrogen density profiles in agreement with SPC/E-modeled water between Pt walls than the SRC. On the charge densities, we recorded a higher surface charge density and capacitance with the LRC compared to those predicted with the SRC model, which implies that SRC underestimated the capacitance of water between graphene walls by 12% when compared with the 5.0 μF/cm^2 predicted with the SPC/E water model. The study generally shows improvement in the surface charge density and capacitance of the graphene-water capacitor, which suggests that the models have a future application in large MD systems (with periodic boundaries) involving composite systems where Coulomb interaction between atoms decays slower than and beyond the imposed cutoff.

This research shows the ability of QEqLR and ReaxFF with LRC to model electrochemical processes in graphene/water capacitor at a more realistic Coulomb interaction description and fosters the processing of the details about the surface charge properties of the devices, indicating that Ewald summation is a more accurate descriptor of Coulomb interactions in electrochemical systems. This approach would describe electrochemical systems with practical electrolyte thickness while conserving the electrostatic effect of charged electrodes throughout the dielectric layer. The methods are applicable to not only capacitors, electrochemical metallization cells, electric double layers, batteries, and emerging memory devices but also to large-scale systems consisting of metal-organic frameworks and solid electrolyte materials that are of current technological interest.

SUPPLEMENTARY MATERIAL

Notes on water density and O and H number density profiles are provided in the supplementary material (DOC). Source codes for the implementation and usage of the method in LAMMPS and example LAMMPS input files (with useful comments in the LRC_CWaterC.in and SRC_CWaterC.in) are provided with a tag LRC_ReaxFF.zip as part of the supplementary material. Included is a README file on how to execute the code and use it in LAMMPS.

ACKNOWLEDGMENTS

We acknowledge Hong Kong Polytechnic University and the Department of Applied Physics for the computing resources.

AUTHOR DECLARATIONS

Conflict of Interest

The authors have no conflicts to disclose.

Author Contributions

Udoka Nwankwo: Formal analysis (lead); Methodology (equal); Validation (equal); Writing – original draft (lead); Writing – review & editing (equal). **Chi-Hang Lam:** Resources (equal); Supervision (equal); Writing – review & editing (equal). **Nicolas Onofrio:** Formal analysis (supporting); Resources (equal); Supervision (equal); Writing – review & editing (equal).

DATA AVAILABILITY

The data that support the findings of this study are available within the article and its supplementary material.

REFERENCES

[1] A. H. Castro Neto, F. Guinea, N. M. R. Peres, K. S. Novoselov, and A. K. Geim, Rev. Mod. Phys. **81**, 109 (2009).
[2] J. H. J. Ostrowski and J. D. Eaves, J. Phys. Chem. B **118**, 530 (2014).
[3] E. Persson and B. Halle, J. Am. Chem. Soc **130**, 1774 (2008).
[4] D. E. Moilanen, I. R. Piletic, and M. D. Fayer, J. Phys. Chem. C **111**, 8884 (2007).
[5] C. Melios, C. E. Giusca, V. Panchal, and O. Kazakova, 2D Mater. **5**, 022001 (2018).
[6] A. Aghigh, V. Alizadeh, H. Y. Wong, M. S. Islam, N. Amin, and M. Zaman, Desalination **365**, 389 (2015).
[7] N. Liu, R. Chen, and Q. Wan, Sensors **19**, 3425 (2019).
[8] A. A. B. Hamra, H. N. Lim, W. K. Chee, and H. M. Huang, Appl. Surf. Sci. **360**, 213 (2016).
[9] A. Härtel, M. Janssen, S. Samin, and R. van Roij, J. Phys.: Condens. Matter **27**, 194129 (2015).
[10] D. Jiang, D. Meng, and J. Wu, Chem. Phys. Lett. **504**, 153 (2011).
[11] R. S. Nicholson, Anal. Chem. **37**, 1351 (1965).

[12] C. Merlet, C. Péan, B. Rotenberg, P. A. Madden, P. Simon, and M. Salanne, J. Phys. Chem. Lett. **4**, 264 (2013).
[13] A. K. Rappé and W. A. Goddard, J. Phys. Chem. **95**, 3358 (1991).
[14] A. Oda and S. Hirono, J. Mol. Struct. THEOCHEM **634**, 159 (2003).
[15] W. J. Mortier, S. K. Ghosh, and S. Shankar, J. Am. Chem. Soc. **108**, 4315 (1986).
[16] D. Mathieu, J. Chem. Phys. **127**, 224103 (2007).
[17] J. Chen and T. J. Martínez, Chem. Phys. Lett. **438**, 315 (2007).
[18] J. Morales and T. J. Martínez, J. Phys. Chem. A **108**, 3076 (2004).
[19] G. Jeanmairet, B. Rotenberg, D. Borgis, and M. Salanne, J. Chem. Phys. **151**, 124111 (2019).
[20] T. Liang, A. C. Antony, S. A. Akhade, M. J. Janik, and S. B. Sinnott, J. Phys. Chem. A **122**, 631 (2018).
[21] H. Nakano and H. Sato, J. Chem. Phys. **151**, 164123 (2019).
[22] J. L. Siepmann and M. Sprik, J. Chem. Phys. **102**, 511 (1995).
[23] N. Onofrio, D. Guzman, and A. Strachan, Nanoscale **8**, 14037 (2016).
[24] N. Onofrio and A. Strachan, J. Chem. Phys. **143**, 054109 (2015).
[25] J. Chmiola, G. Yushin, Y. Gogotsi, C. Portet, P. Simon, and P.-L. Taberna, Science **313**, 1760 (2006).
[26] C. Merlet, C. Péan, B. Rotenberg, P. A. Madden, B. Daffos, P.-L. Taberna, P. Simon, and M. Salanne, Nat. Commun. **4**, 1 (2013).
[27] Z. Li, G. Jeanmairet, T. Méndez-Morales, B. Rotenberg, and M. Salanne, J. Phys. Chem. C **122**, 23917 (2018).
[28] D. T. Limmer, Phys. Rev. Lett. **115**, 256102 (2015).
[29] J. Le Ma, Q. Meng, and J. Fan, Phys. Chem. Chem. Phys. **20**, 8054 (2018).
[30] C. Merlet, D. T. Limmer, M. Salanne, R. van Roij, P. A. Madden, D. Chandler, and B. Rotenberg, J. Phys. Chem. C **118**, 18291 (2014).
[31] O. Borodin, X. Ren, J. Vatamanu, A. von Wald Cresce, J. Knap, and K. Xu, Acc. Chem. Res. **50**, 2886 (2017).
[32] D. Laage and J. T. Hynes, Science **311**, 832 (2006).
[33] T. Ohto, H. Tada, and Y. Nagata, Phys. Chem. Chem. Phys. **20**, 12979 (2018).
[34] G. Stirnemann, F. Sterpone, and D. Laage, J. Phys. Chem. B **115**, 3254 (2011).
[35] R. Smith, K. Jolley, C. Latham, M. Heggie, A. van Duin, D. van Duin, and H. Wu, Nucl. Instrum. Methods Phys. Res. B **393**, 49 (2017).
[36] C. E. Wilmer and R. Q. Snurr, J. Chem. Eng. **171**, 775 (2011).
[37] J. N. Louwen and E. T. C. Vogt, J. Mol. Catal. A Chem. **134**, 63 (1998).
[38] H. M. Aktulga, S. A. Pandit, A. C. T. van Duin, and A. Y. Grama, SIAM J. Sci. Comput. **34**, C1 (2012).
[39] E. M. Pierce, P. Frugier, L. J. Criscenti, K. D. Kwon, and S. N. Kerisit, Int. J. Appl. Glass Sci. **5**, 421 (2014).
[40] I. Jomaa, N. Issaoui, T. Roisnel, and H. Marouani, J. Mol. Struct. **1242**, 130730 (2021).
[41] G. Saleh, C. Gatti, L. L. Presti, and J. Contreras-García, Chem. Eur. J. **18**, 15523 (2012).
[42] H. Schreiber and O. Steinhauser, BioChemistry **31**, 5856 (1992).
[43] M. P. Allen and D. J. Tildesley, *Computer Simulation of Liquids* (Oxford University Press, New York, 2017).
[44] D. Frenkel and B. Smit, *Understanding Molecular Simulation: From Algorithms to Application* (Academic Press, San Diego, CA, 2002).
[45] A. P. Thompson, Comput. Phys. Commun. **271**, 108171 (2022).
[46] B. Hess, C. Kutzner, D. van der Spoel, and E. Lindahl, J. Chem. Theory Comput. **4**, 435 (2008).
[47] J. C. Phillips, R. Braun, W. Wang, J. Gumbart, E. Tajkhorshid, E. Villa, C. Chipot, R. D. Skeel, L. Kael, and K. Schulten, J. Comput. Chem. **26**, 1781 (2005).
[48] D. S. Shamshirgar, J. Bagge, and A.-K. Tornberg, J. Chem. Phys. **154**, 164109 (2021).
[49] J. Kolafa and J. W. Perram, Mol. Simul. **9**, 351 (1992).
[50] H. G. Petersen, J. Chem. Phys. **103**, 3668 (1995).
[51] Y. Kim, A. C. T. van Duin, and J. D. Kubicki, J. Mater. Res. **28**, 513 (2013).
[52] U. Nwankwo, Y.-D. Wang, C. H. Lam, and N. Onofrio, J. Chem. Phys. **159**, 044104 (2023).
[53] I.-C. Yeh and M. L. Berkowitz, J. Chem. Phys. **110**, 7935 (1999).
[54] Y. Zhang, G. Stirnemann, J. T. Hynes, and D. Laage, Phys. Chem. Chem. Phys. **22**, 10581 (2020).
[55] B. Demir and D. Searles, Nanomaterials **10**, 2181 (2020).
[56] Z. Wang, Y. Yang, D. L. Olmsted, M. Asta, and B. B. Laird, J. Chem. Phys. **141**, 184102 (2014).
[57] M. V. Fedorov and A. A. Kornyshev, Chem. Rev. **114**, 2978 (2014).
[58] A. P. Willard, S. K. Reed, P. A. Madden, and D. Chandler, Faraday Discuss. **141**, 423 (2009).
[59] R. Parsons, Pure Appl. Chem. **37**, 499 (1974).
[60] A. A. Kornyshev, J. Phys. Chem. B **111**, 5545 (2007).
[61] D. T. Limmer, C. Merlet, M. Salanne, D. Chandler, P. A. Madden, R. van Roij, and B. Rotenberg, Phys. Rev. Lett. **111**, 106102 (2013).
[62] Y. Liu, W. Liu, Z. Wang, W. He, Q. Tang, Y. Xi, X. Wang, H. Guo, and C. Hu, Nat. Commun. **11**, 1599 (2020).
[63] S. Li, Y. Huang, D. Min, G. Qu, H. Niu, Z. Li, W. Wang, J. Li, and W. Liu, Sci. Rep. **9**, 5464 (2019).
[64] G. I. Guerrero-García, E. González-Tovar, M. Chávez-Páez, J. Kłos, and S. Lamperski, Phys. Chem. Chem. Phys. **20**, 262 (2018).
[65] L. A. Bade, J. O. Dennis, M. H. Md Khir, and W. P. Wen, "Design of tunable interdigital capacitor," J. Phys.: Conf. Ser. **1123**, 012008 (2018).
[66] Z. Wang, D. L. Olmsted, M. Asta, and B. B. Laird, J. Phys.: Condens. Matter **28**, 464006 (2016).
[67] J. N. Sachs, P. S. Crozier, and T. B. Woolf, J. Chem. Phys. **121**, 10847 (2004).
[68] G. Feng, J. S. Zhang, and R. Qiao, J. Phys. Chem. C **113**, 4549 (2009).
[69] C. Merlet, M. Salanne, B. Rotenberg, and P. A. Madden, J Chem. Chem. C **115**, 16613 (2011).
[70] G. Feng, R. Qiao, J. Huang, S. Dai, B. G. Sumpter, and V. Meunier, Phys. Chem. Chem. Phys. **13**, 1152 (2011).
[71] S. A. Kislenko, I. S. Samoylov, and R. H. Amirov, Phys. Chem. Chem. Phys. **11**, 5584 (2009).